Exploring aliovalent substitutions in the lithium halide superionic conductor $Li_{3-x}In_{1-x}Zr_xCl_6$ ($0 \leq x \leq 0.5$)

Bianca Helm,[a] Roman Schlem,[a] Björn Wankmiller,[a,b,c] Ananya Banik,[a] Ajay Gautam,[d] Justine Ruhl,[d] Cheng Li,[e] Michael Ryan Hansen,[b] and Wolfgang G. Zeier*[a,f]

[a]*Institute of Inorganic and Analytical Chemistry, University of Münster, Correnstrasse 30, D-48149 Münster, Germany.*

[b]*Institute of Physical Chemistry, University of Münster, Correnstrasse 30, D-48149 Münster.*

[c]*International Graduate School for Battery Chemistry, Characterization, Analysis, Recycling and Application (BACCARA), University of Münster, Corrensstrasse 40, D-48149 Münster, Germany*

[d]*Institute of Physical Chemistry, Justus-Liebig-University Giessen, Heinrich-Buff-Ring 17, D-35392 Giessen, Germany.*

[e]*Neutron Scattering Division, Oak Ridge National Laboratory (ORNL), 1 Bethel Valley Road, Oak Ridge, Tennessee 37831-6473, United States.*

[f]*Helmholtz Institut Münster, FZ Jülich, Corrensstrasse 46, D-48149 Münster, Germany.*

*wzeier@uni-muenster.de

Abstract

In recent years, ternary halides Li_3MX_6 (M = Y, Er, In; X = Cl, Br, I) have garnered attention as solid electrolytes due to their wide electrochemical stability window and favorable room-temperature conductivities. In this material class, the influences of iso- or aliovalent substitutions are so far rarely studied in-depth, despite this being a common tool for correlating structure and transport properties. In this work, we investigate the impact of Zr substitution on the structure and ionic conductivity of Li_3InCl_6 ($Li_{3-x}In_{1-x}Zr_xCl_6$ with $0 \leq x \leq 0.5$) using a combination of neutron diffraction, nuclear magnetic resonance and impedance spectroscopy. Analysis of high-resolution diffraction data shows the presence of an additional tetrahedrally coordinated lithium position together with cation site-disorder, both of which have not been reported previously for Li_3InCl_6. This Li^+ position and cation disorder lead to the formation of a three-dimensional lithium ion diffusion channel, instead of the expected two-dimensional diffusion. Upon Zr^{4+} substitution, the structure exhibits non-uniform volume changes along with an increasing number of vacancies, all of which lead to an increasing ionic conductivity in this series of solid solutions.

1. Introduction

All-solid-state batteries are considered to be promising candidates for a safe and stable energy storage system offering rigidity, high energy densities and reduced risk of flammability. In addition, the energy density of all-solid-state batteries can be enhanced by about 70% when using Li metal as an anode.[1] The application of solid electrolytes improve the battery not only in terms of reduced risk of combustion, compared to liquid electrolytes, but also by enabling battery use at a wider temperature range and higher current densities for operation.[1,2] The search for the replacement of liquid electrolytes led to the discovery of several promising solid electrolytes including garnets,[3–5] $Li_{10}GeP_2S_{12}$[6–8], argyrodites[9–11] and *thio*-LISICONs[12–15], all of which were investigated thoroughly by iso- or aliovalent substitutions to determine influences on ionic transport, for instance the width of diffusion pathway,[5,16,17] lattice polarizability[9,18,19] or Li^+/vacancy density.[13,20–22] Recently, the ternary halide electrolytes Li_3MX_6 (M = Y, Er, In, Sc and X = Cl, Br, I) have drawn attention for exhibiting conductivities in the $mS \cdot cm^{-1}$ - range at room temperature in combination with an enhanced electrochemical stability compared to the sulfide electrolytes.[23–29]Additionally, halide materials are promising candidates as cathode electrolytes due to their oxidation stability.[18,26,30] Schlem *et al*., showed that the conductivity of Li_3ErCl_6, Li_3YCl_6, and Li_3YBr_6 is strongly dependent on a cation site-disorder that is affected by the synthesis conditions, enabling tailoring of the energy landscape for lithium ion diffusion.[29,31] Moreover, studies showed that the heat treatment conditions strongly influence the ionic conductivity.[31,32] Just recently, Kwak *et al.* showed that a mechanochemical synthesis stabilizes the trigonal structure for Li_2ZrCl_6, while annealing resulted in a monoclinic structure exhibiting conductivities of $0.4\ mS \cdot cm^{-1}$ and $5.7 \cdot 10^{-3}\ mS \cdot cm^{-1}$, respectively.[33] The conductivity of mechanochemically prepared Li_2ZrCl_6 was further enhanced up to $\sim 1\ mS \cdot cm^{-1}$ by Fe^{3+} substitution. The introduction of Zr^{4+} in Li_3ErCl_6 and Li_3YCl_6 resulted in a conductivity increase by more than one order of magnitude by introducing vacancies into the structure.[26] Additionally, increasing the zirconium content induced a change in the crystal structure from a trigonal to orthorhombic structure,[26] which was originally proposed by Steiner *et al.*[34] for the pristine Li_3YCl_6. In contrast to the aliovalent substitutions, phase transitions were observed for the isovalent substitution series $Li_3Y_{1-x}In_xCl_6$ changing from an orthorhombic to the trigonal phase for Li_3YCl_6 when exceeding a substitution degree of $x(In) = 0.1$ and then, adapting the monoclinic structure of Li_3InCl_6 for $x(In) \geq 0.3$.[35] Interestingly and advantageously, Li_3InCl_6 is fully recoverable after humidity exposure and synthesizable *via* a water-mediated route resulting in a conductivity of $\sim 2\ mS \cdot cm^{-1}$ at 25 °C.[25,35,36] Common high-temperature or mechanochemical synthesis of Li_3InCl_6 results in comparable room-temperature

conductivities of ~1.5 mS·cm^{-1}.[24,35] Li_3InCl_6 adapts a monoclinic structure (space group: *C*2/*m*) and was initially solved from single crystal X-ray diffraction by Schmidt *et al.*[37] It crystallizes in a layered structure consisting of edge-sharing $(InCl_6)^{3-}$ and $(LiCl_6)^{5-}$ octahedra. The $(InCl_6)^{3-}$ octahedra are exclusively located within the (001) lattice plane, whereas $(LiCl_6)^{5-}$ octahedra can be found within the (002) lattice plane (Figure 1a). More precisely, indium occupies the Wyckoff 2*a* (M1) and lithium occupies the Wyckoff 4*h* (Li1) and Wyckoff 2*d* (Li2) position (see Figure 1b and 1c).[37] Further, this work will show mixed indium - lithium octahedra within the (001) lattice plane, i.e. the Wyckoff 4*g* (M2/Li4) position. In each lattice plane, the octahedra of the Wyckoff position with a fourfold multiplicity are directly connected with each other, forming a network based on a honeycomb pattern, while the positions with lower multiplicity are isolated from each other. Similar to the recently found Li^+ substructure in Li_3YBr_6,[31,38] this work suggests that lithium occupies two additional positions, namely the already mentioned M2/Li4, as well as Wyckoff 8*j* (Li3). These new positions introduce a cation site-disorder within the (001) lattice plane and a four-fold coordinated lithium position in the (002) lattice plane. The lithium octahedral connectivity is shown in Figure 1d to illustrate the three-dimensional connectivity within the structure. All shown lithium octahedra are face-sharing with the tetrahedral position Li3, making the latter essential for ionic conductivity as the Li3 position then likely resembles a transition state for ionic motion.[39,40]

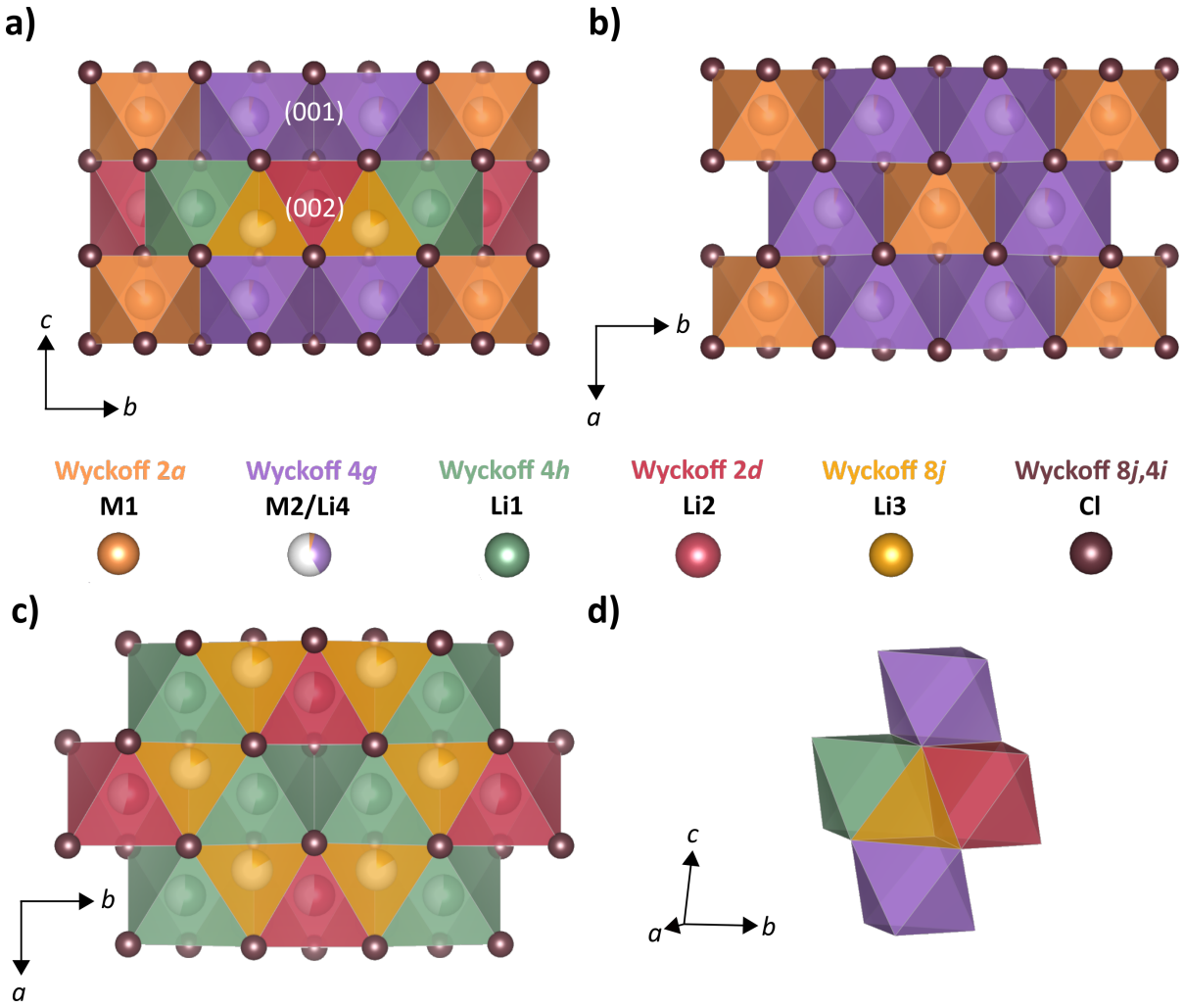

Figure 1: (a) Li_3InCl_6 structure showing the $(InCl_6)^{3-}$ octahedra in the (001) lattice plane and $(LiCl_6)^{5-}$ octahedra and a tetrahedral site in the (002) lattice plane. (b) View along the c-axis, showing the arrangement of edge-sharing $(InCl_6)^{3-}$ octahedra along the (001) lattice plane. The M2/Li4 positions are directly connected to each other forming a honeycomb-like network, while the M1 sites are isolated from each other. Additionally, the M2/Li4 position was found to be cation-disordered with a lithium occupancy about six times higher than indium occupancy for Li_3InCl_6. (c) Illustration of the lithium substructure is shown as reported consisting of edge-sharing $(LiCl_6)^{5-}$ octahedra in the (002) lattice plane. Moreover, lithium occupies a tetrahedral Li3 position. The display along the c-axis reveals a similar arrangement of lithium polyhedra as the indium polyhedra in (001) lattice plane. The Li1 site forms a network while the Li2 site is encircled by the six Li1 octahedra. (d) Cut-out of lithium substructure showing the three-dimensional connectivity of lithium octahedra including the tetrahedral lithium position.

The recent success of zirconium addition in these halide based ionic conductors[26,33] encouraged us to investigate the $Li_{3-x}In_{1-x}Zr_xCl_6$ ($0 \leq x \leq 0.5$) series of solid solutions expecting a positive impact on ionic transport by tuning the Li^+ carrier density. Moreover, the similar radii of indium

and zirconium cations ($r(In^{3+})$ = 0.80 Å and $r(Zr^{4+})$ = 0.72 Å)) suggested the possibility that zirconium could be successfully incorporated into the structure.[41] Additionally, *ab initio* molecular dynamics calculations showed that $Li_{2.5}In_{0.5}Zr_{0.5}Cl_6$ should not only be stable but also exhibit an improved conductivity compared to Li_3InCl_6.[42] Within the halide solid electrolytes the aliovalent substitutions are scarce, therefore in order to assess their impact on structure and ionic transport, a combination of neutron diffraction, nuclear magnetic resonance and impedance spectroscopy was used. The incorporation of zirconium compresses the unit cell in *c*-direction and results in non-uniform polyhedral volume changes indicating structural distortions. The removal of lithium ions improves the conductivity by almost one order of magnitude. In addition, the Li^+ substructure that is found here suggests the opportunity of three-dimensional diffusion. Thus, this work aims to further strengthen the understanding of structure-property relationships within the material class of lithium-ion conducting rare-earth halides.

2. Experimental Section

Synthesis. All the synthesis steps were carried out under Ar atmosphere. $Li_{3-x}In_{1-x}Zr_xCl_6$ ($0 \leq x \leq 0.5$) was prepared *via* mechanochemical synthesis in a planetary mill followed by an annealing step. The precursors LiCl (ChemPur, 99.99 %), $ZrCl_4$ (99.5 %, metal basis, Alfa Aesar) and $InCl_3$ (99.999 %, trace metal basis, Sigma Aldrich) were placed stoichiometrically in a ball-mill cup. The powder to milling-media ratio was 1:20 with a milling media diameter of 5 mm. The powders were mixed for 99 cycles in reverse mode. One cycle includes mixing at 500 rpm for 15 min with a subsequent 5 min break for cooling. Then, the powders were pelletized with a hand press and transferred into an ampoule that was pre-dried at 800 °C under dynamic vacuum. The ampoules were sealed and placed into a pre-heated furnace (260 °C). After four hours of annealing at 260 °C, the samples were air-quenched. The colorless pellets were hand-ground into powders and used for subsequent characterizations.

Powder X-ray diffraction. X-ray diffraction was performed on a PANalytical Empyrean diffractometer in Bragg-Brentano θ-θ geometry with a PIXcel^{3D} detector. Cu K_α radiation (λ = 1.54 Å) was used with an anti-scatter slit of 1°, a step size of 0.026° within a 2θ-range of 10° to 90°. The powders were placed on (911)-oriented silicon zero background sample holders and were sealed air-tight with a 7.5 µm thick Kapton polyimide film.

Neutron powder diffraction. Neutron powder diffraction data of $Li_{3-x}In_{1-x}Zr_xCl_6$ ($0 \leq x \leq 0.5$) were collected at Oak Ridge spallation neutron source (SNS, Oak Ridge National Laboratory) using the PAC automatic sample changer at POWGEN diffractometer (BL-11A beamline). Under inert conditions, the samples (~ 2 g) were loaded into a cylindrical vanadium can (Ø = 6 mm) which was sealed with a copper gasket to avoid exposure to air during the measurement. The diffractograms were collected for four hours in high-resolution mode at room temperature using a single bank with a center wavelength of 1.5 Å.

Rietveld analysis. The absorption-corrected neutron diffractograms were analyzed using the TOPAS Academics V6 software package.[43] Starting point of the refinement was the reported Li_3InCl_6 single crystal structure from Schmidt *et al*.[37] First, the refinement included (1) the background, (2) scaling factors of main and side phase, (3) lattice parameters and angle beta and (4) peak-shape function, which was a convolution of a pseudo-Voigt and GSAS back-to-back exponential function to obtain a good profile fit.[44] Furthermore, (5) the crystal structure itself was refined, starting by refining the thermal displacement parameters, occupancies and coordinates of non-Li species, In and Cl. In order to reduce the number of free variables, the In occupancy was constrained to the nominal In content after a few refinement cycles without

constraints as it remained constant. After refinement of the immobile framework, (6) the Li thermal displacements, occupancies and coordinates were refined while keeping all other atoms fixed. Similar to In, the Li content was fixed to the nominal stoichiometry. (7) Every non-Li octahedral and tetrahedral position was evaluated for possible Li occupancy. Besides the already known two Li octahedral positions (Li1 and Li2) in the (002) lattice plane, Li was found to occupy a tetrahedral position Li3 within the (002) lattice plane. Nevertheless, the coordinates of this additional position cannot be refined freely since it resulted in a displacement of Li out of the tetrahedra, suggesting a rather unstable site (see Results and Discussion). For other vacant tetrahedral position in the (001) and (002) lattice plane, some Li occupancy was found but a negative thermal displacement parameter was then associated with this site. The negative thermal displacement suggests no occupancy and therefore, these positions were neglected. During the separate refinement of the mobile and immobile species, In is located on two crystallographic positions (M1 and M2/Li4) within the (001) plane, whereas three different positions (Li1, Li2 and Li3) can be found for lithium in the (002) plane. (8) In the final step, all In, Cl and Li thermal displacement parameters, occupancies and coordinates were refined together except the coordinates of Li3 site. The combined refinement of the mobile and immobile structural features proved some instability at first, especially of the M2/Li4 site that was only occupied by In at this point. Therefore, Li was placed on the M2/Li4 site, which resulted in physically reasonable thermal displacement parameters (Table S2) and stable refinements. Other Li/In disorders were also explored, nevertheless the combined Li/In occupancy on M2/Li4 site provided the most stable structural model and lowest refinement statistics. (9) The found structural model of Li_3InCl_6 was applied on the zirconium substitution series assuming zirconium replaces indium on its crystallographic sites. The indium-zirconium-ratio was always fixed to nominal stoichiometry. The fits of neutron diffractograms, the structural parameters as well as the crystallographic information files (CIFs) are reported in the supporting information (Figure S2, Table S1-S7).

Electrochemical impedance spectroscopy. Ionic conductivities were measured by AC impedance spectroscopy. Approximately 150 mg of each sample were filled into press cells with a PEEK inlet[45] and subsequently pressed uniaxially with 374 MPa for three minutes followed by a slow pressure release. All obtained geometrical pellet densities were around 84 %. The impedance measurements were performed with a SP300 impedance analyser (Biologic) in a temperature range of 233 K to 333 K and within a frequency range of 7 MHz to 100 mHz applying an amplitude of 10 mV. The spectra analyses were carried out with the

RelaxIS 3 software (rhd instruments). The measurement uncertainty of conductivity and activation energy were calculated from the fit errors and geometrical uncertainties of the pellet.

Nuclear magnetic resonance spectroscopy. Static saturation recovery ^{7}Li NMR experiments were performed on a Bruker AVANCE III 300 spectrometer equipped with a widebore magnet which operates at 300 MHz (7.05 T) using a VTN broadband probe. The powder samples were transferred into cylindrical zirconia rotors with an outer diameter of 4 mm under Ar atmosphere. All experiments were conducted at a Larmor frequency of 116.6 MHz with a pulse length of 2.5 µs for a 90° pulse corresponding to a nutation frequency of 100 kHz. The length of the recovery delay was incremented with four steps per decade from $t_1 = 10^{-5}$ s to $t_{28} = 56.234$ s. The Fourier transformed signals were integrated in TopSpin and the signal intensity curves were fitted using an exponential saturation function with a stretching exponent. The temperature of the sample was regulated via a nitrogen gas flow and electrical heating. In the temperature range between 200 K and 290 K an *Air Jet XR* compressor-based cooling system from SP Scientific (FTS Systems) was used; from 320 K to 440 K an uncooled nitrogen gas flow was employed to stabilize the temperature. ^{1}H NMR spectra of methanol (200 K to 290 K) and ethylene glycol (320 K to 440 K) were recorded separately to calibrate the temperature with the occurring shifts in signal frequency.

Bond valence sum calculations. The bond valence sum (BVS) was calculated by using the softBV V1.2.1 program.[46,47] The BVS was calculated for a variation of the determined Li_3InCl_6 structure with a screening factor of 0.642187 and a resolution of 0.1. It was not possible to perform the calculations with having a site disorder on M2/Li4 (Wyckoff 4*g*) site. Therefore, calculations were performed after removing the indium from M2/Li4 site and charge neutrality was assured by adapting the indium occupancy on M1 site.

3. Results and Discussion

Influences of synthesis on the host-framework structure. To explore the influence of zirconium incorporation into Li_3InCl_6, the series of solid solutions $Li_{3-x}In_{1-x}Zr_xCl_6$ ($0 \leq x \leq 0.5$) was prepared using mechanochemical syntheses. The laboratory X-ray diffraction patterns (Figure S1) indicate that LiCl is present as a minor impurity in almost every composition along the series. Minor side phases, probably correlated to In and Zr, with low intensities in the diffraction patterns can be observed but cannot be assigned to any specific compound. Up to a zirconium content of $x(Zr) = 0.5$ crystalline phases are obtained. Nevertheless, as shown in Figure S1, the strong broadening of the reflections at $x(Zr) = 0.6$, indicates a decreased crystallinity and hence, the material exhibits just short-range order within the employed synthesis conditions. Therefore, in this work, only the compositions of $Li_{3-x}In_{1-x}Zr_xCl_6$ with $x(Zr) \leq 0.5$ are further analyzed for their structure and transport properties.

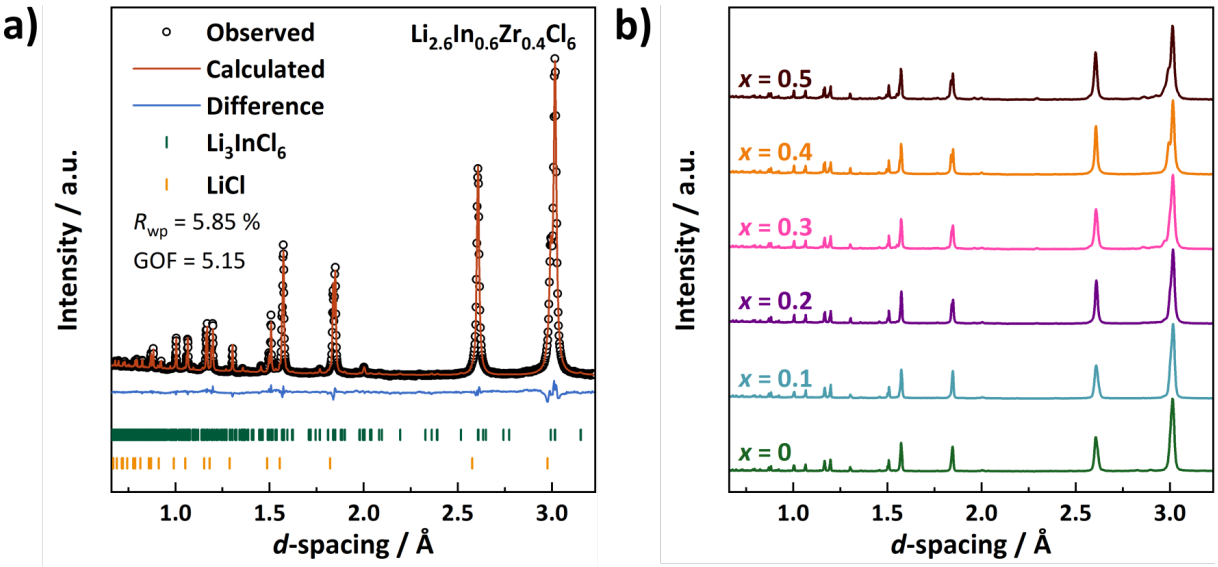

Figure 2: (a) Representative Rietveld refinement of room temperature neutron diffraction data of $Li_{2.6}In_{0.6}Zr_{0.4}Cl_6$. A minor impurity phase of LiCl (1.13 (7) wt.%) can be found. (b) Display of all $Li_{3-x}In_{1-x}Zr_xCl_6$ neutron diffractograms.

Rietveld refinements against neutron diffraction data are employed to explore the structural changes upon zirconium incorporation. Figure 2a shows a representative Rietveld refinement and Figure 2b summarizes all collected neutron diffraction data. All other refinements and the corresponding structures are shown in the Supporting Information. In the neutron diffraction data, LiCl can be found as a minor impurity with average amounts of 2 wt.%. Whereas there are no strong changes in the neutron diffraction data at first glance, the shoulder of one reflection at around 3 Å seemingly shifts to lower *d*-spacings suggesting subtle changes in the lattice. Figure 3a shows the changes to the unit cell as obtained from the neutron diffraction

data refinements. A decreasing volume of the unit cell can be observed with incorporation of zirconium, which may be due to the difference in ionic radii ($r(Zr^{4+}) = 0.72$ Å < $r(In^{3+}) = 0.8$ Å)[41] or due to the changing overall lithium composition. This decrease in volume seems mainly driven by the compression of the unit cell along *c*-direction, while the lattice parameters *a* and *b* remain nearly unchanged. This asymmetric shrinkage was also observed by Kwak *et al.* when comparing Li_3InCl_6 and Li_2ZrCl_6 diffraction patterns.[33]

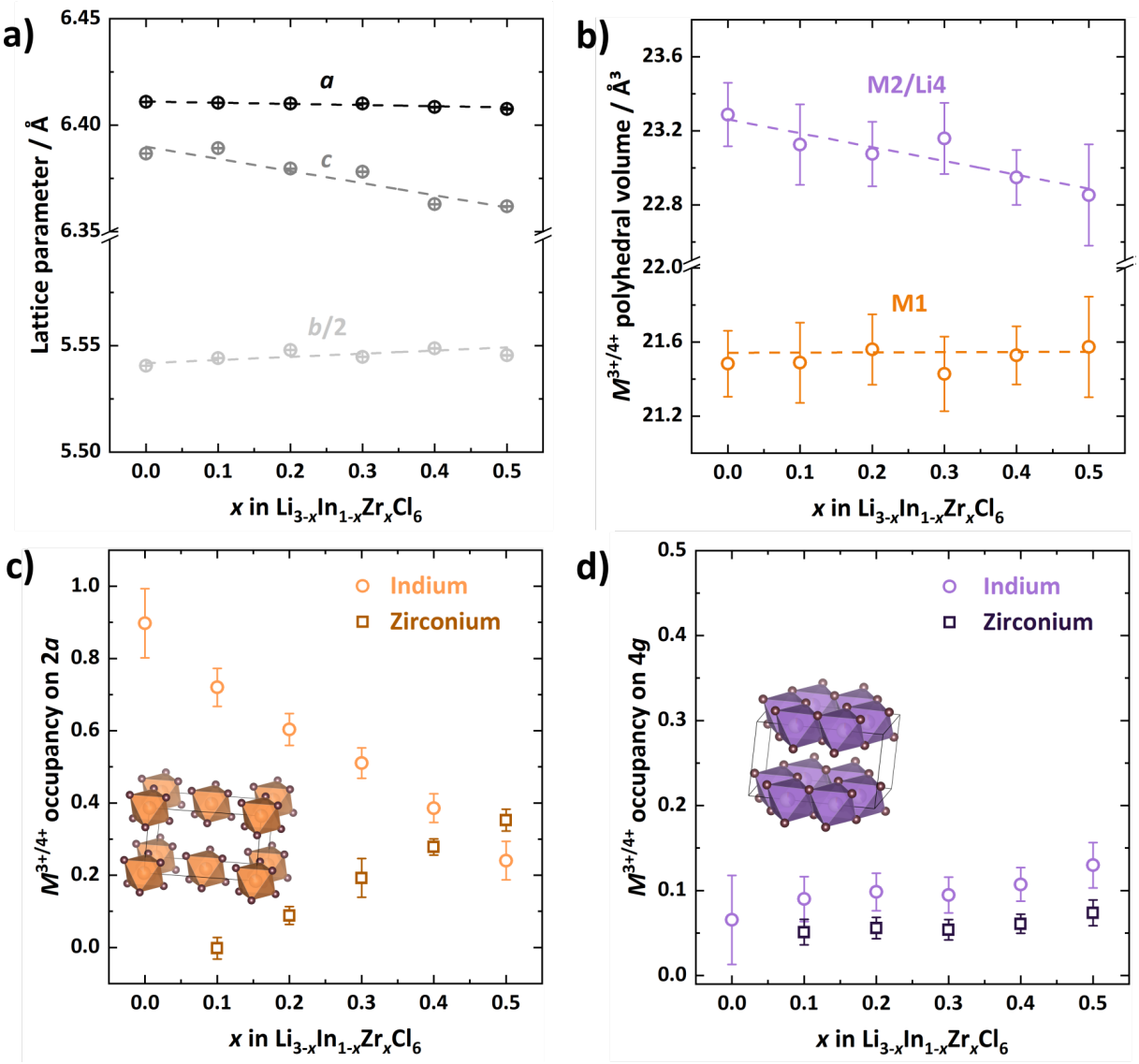

Figure 3: (a) The lattice parameter a and b (here depicted as b/2) stay almost constant while the lattice parameter c is decreasing. (b) The polyhedral volume on the M1 site stays constant while the polyhedral volume on the M2/Li4 position decreases slightly by about 2 %. (c) Evolution of indium-zirconium-ratio on M1 site is depicting a linear change in occupancy. (d) The indium-zirconium-ratio seems to remain unchanged on the M2/Li4 site over the series. The lines are guides-to-the-eye.

Using the structural data, it is possible to observe changes in occupancies and polyhedral volumes. The polyhedral volume of the M1 position seems to remain constant during the substitution while the polyhedral volume on the M2/Li4 position is decreasing slightly (see Figure 3b). Monitoring the occupancy of indium and zirconium on M1 and M2/Li4 position, it is obvious that the defect M2/Li4 position seems to be less favored for occupation than the M1 site. The occupancy of zirconium gradually increases on the M1 site with a concurrent decrease in indium occupancy while the fractions of indium and zirconium on M2/Li4 site stay comparably low over the whole substitution range (see Figure 3c and 3d). From an electrostatic point of view, the M1 position may be more reasonable to be occupied by zirconium because these octahedral positions are not directly connected to each other. This lack of direct connection expresses a larger distance, possibly reducing Coulombic repulsion. Further on, the octahedron on the M1 site is smaller than the octahedron on M2/Li4 site, potentially being more favorable for the smaller Zr^{4+}. The distribution of indium and zirconium on the M1 and M2/Li4 sites seem reasonable considering the sizes and charges, however the volume change of the two sites is unequal. The unit cell is compressed along the *c*-direction, which would suggest an even reduction of both octahedral volumes especially of the M1 and M2/Li4 site in the (001) lattice plane.

Lithium sublattice. To understand the influence of zirconium substitution on the lithium substructure and the associated diffusion pathway, lithium polyhedral volumes and occupancies are further evaluated (see Figure 4). Besides the already known two lithium octahedral positions[37] Li1 and Li2 in the (002) lattice plane, lithium was found to occupy a tetrahedral position Li3 in the (002) lattice plane indicated by an occupancy of 17 (1) % and reasonable thermal displacement of 1.8 (6) $Å^2$ in Li_3InCl_6. In contrast to the Li^+ substructure in Li_3YBr_6,[31,38] here the additional lithium is found in the (002) and not within the (001) lattice plane. In addition, a mixed occupancy of lithium and indium on the M2/Li4 position can be found and structurally this site contains the ions In^{3+}, Zr^{4+}, Li^+ as well as vacancies. The lithium polyhedral volumes on Li1 and Li2 position are slightly altered when introducing zirconium into the crystal structure with an increase in the Li1 volume and a decrease in Li2 polyhedral volume (see Figure 4a). In addition, the octahedral volume of the M2/Li4 site is shrinking as discussed above. Note that lithium is distributed over four sites within Li_3InCl_6. Increasing the zirconium content leads to the loss of occupancy on the tetrahedral position Li3 (see Figure 4a and 4b) and as a consequence, lithium occupies just the octahedral positions Li1, Li2 and M2/Li4 with $x(Zr) \geq 0.1$. In line with the unstable refinements of the tetrahedral Li3 position

for Li_3InCl_6, this suggests the tetrahedral position to be an intermediate higher energy site that is depopulated first when Li^+ is removed from the system. The lithium ions seem to preferably occupy the cation disordered M2/Li4 position instead of the Li1 and Li2 positions where the occupancy gradually decreases with increasing zirconium amount. On average the lithium-metal ratio on the M2/Li4 position is about five (see Figure S3). In particular, this means that five times more lithium ions than metal ions occupy this position. Thus, within this structural model the M2/Li4 position belongs mainly to the lithium sublattice and therefore, may be considered as just a minor part of the host-framework in which some In/Zr occupy the Li^+ diffusion pathways.

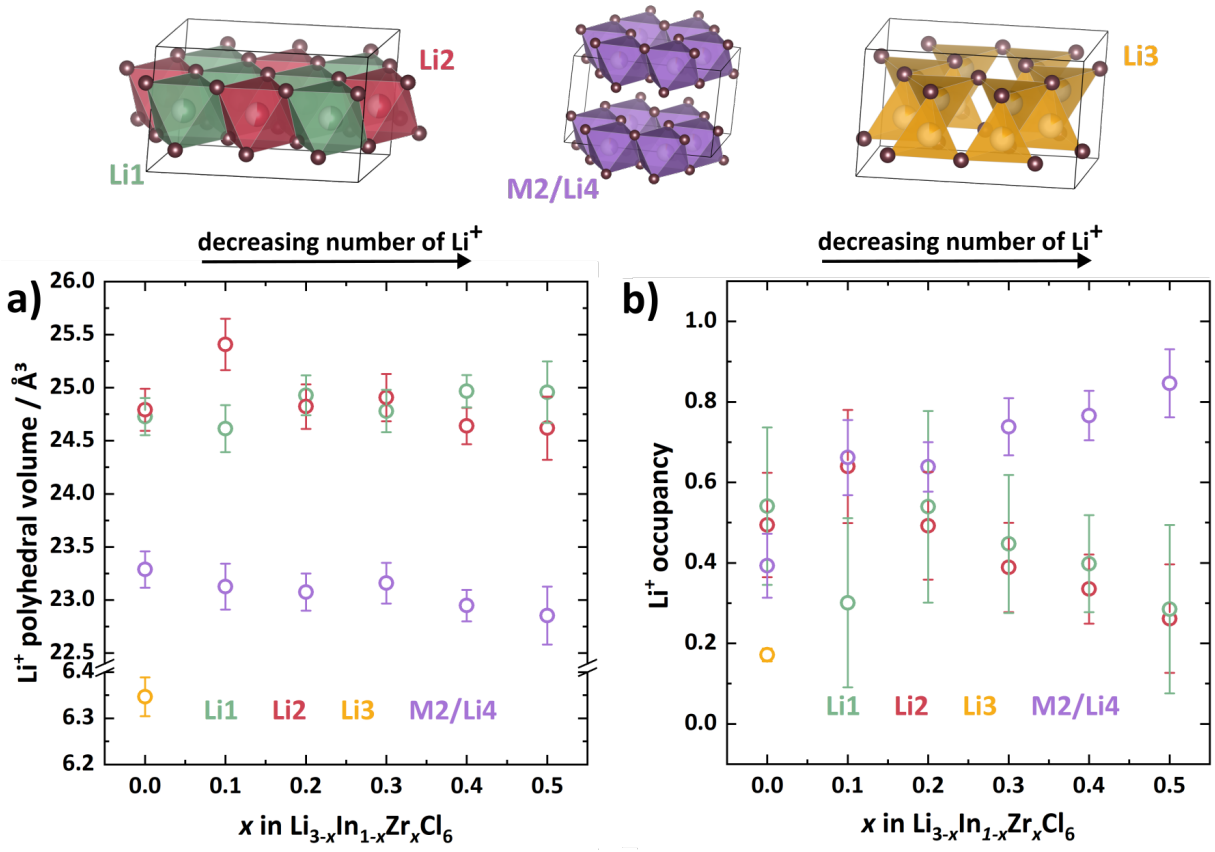

Figure 4: (a) Lithium polyhedral volumes in $Li_{3-x}In_{1-x}Zr_xCl_6$ with the different lithium sites shown above. Only in Li_3InCl_6, lithium was found on the tetrahedral site. (b) Lithium occupancies with increasing zirconium content exhibit an occupancy preference of lithium on M2/Li4 site.

Structural correlations. The host-framework and lithium sublattice both exhibit some peculiarities within their structural evolution upon zirconium substitution, which need to be evaluated together. The non-uniform shrinkage of the unit cell, which is indicated by the reduction in lattice parameter *c* and unequal polyhedral changes, may be due to local structural distortions. The latter can lead to unexpected behavior and certain decoupling of polyhedral

volumes from each other, as recently found in other alkaline rare-earth halides, Na_3ErCl_6, Li_3ErCl_6 and Li_3YBr_6.[29,48] These distortions within the structure can be rationalized based on the polyhedral changes (see Figure 5a).

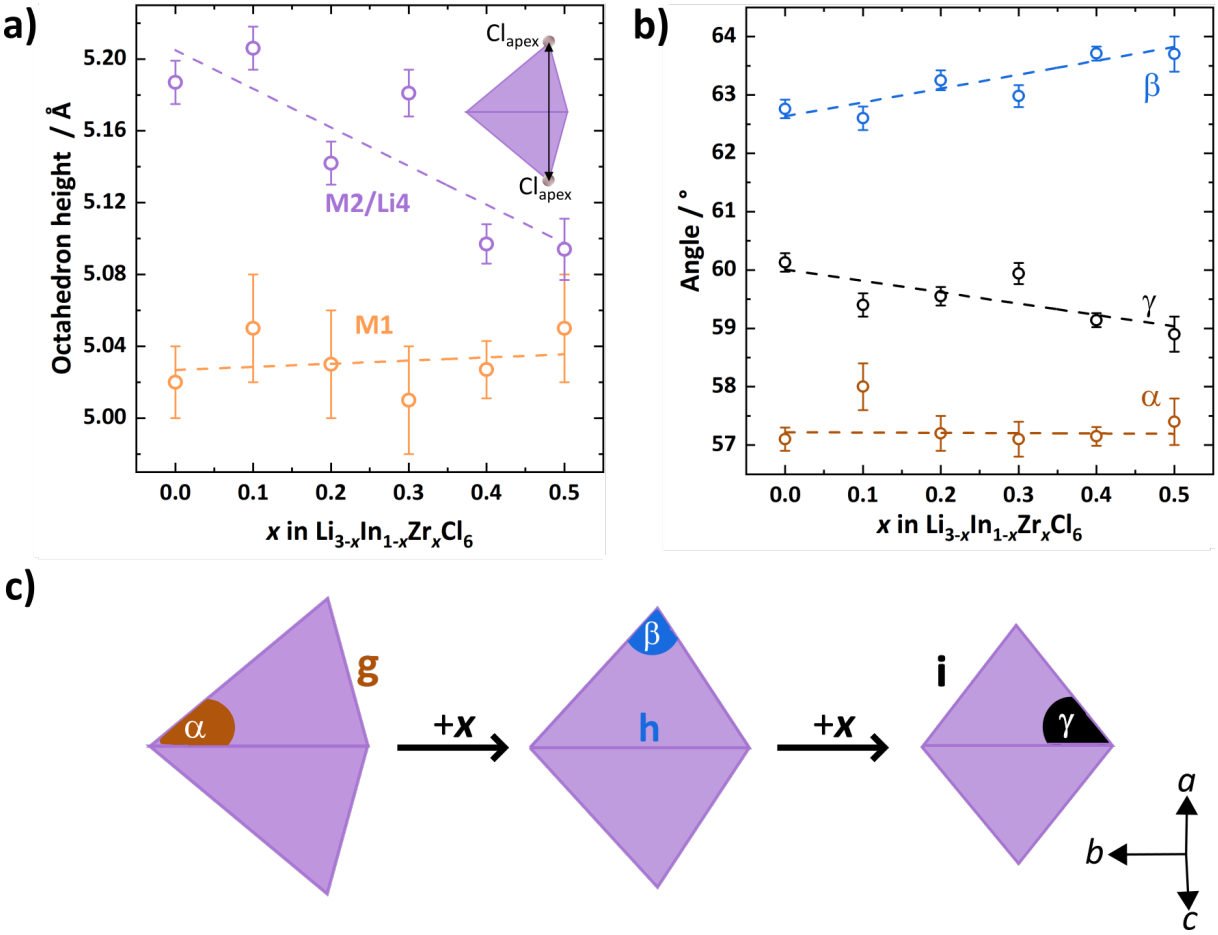

Figure 5: (a) The octahedron height, distance of apical chlorides (see inset), of M2/Li4 site is decreasing while the height of the octahedron of M1 site is nearly constant. (b) Illustration of the angle evolution of the triangular face with zirconium substitution. The angles are color coded and marked in (c). (c) Display of an exaggerate distortion of the octahedron of M2/Li4 site. Upon zirconium substitution, corresponding to an increasing x value, the distortion of the octahedron on M2/Li4 site changes by the shift of the apical chlorides. The lines are guides-to-the-eye.

The height of the distorted MCl_6 octahedra, representing the distance of the apical chloride positions (see inset Figure 5a), of the M2/Li4 site decreases, while the octahedron height of M1 site stays almost constant. Therefore, the changes in polyhedral volume within the (001) lattice plane seems to be mainly driven by these height changes, since the residual edge lengths do not change significantly (Figure S4a and S4b). In addition, the zirconium substitution induces an average symmetry change of the distorted octahedron on M2/Li4 site, which alters the degree

of distortion, as illustrated in Figure 5c. The apex chlorides are moving more towards the center and the height is being reduced. The movement of the apex chlorides can be visualized by monitoring the angles within a triangular face of the octahedron of the M2/Li4 position (Figure 5b). The angle β increases with a concurrent decrease in angle γ. The edge lengths *a* and *c* decrease and seem to run against a similar value, indicated by the varying degrees of length changes for *g* and *i*, while the edge *h* stays constant (Figure S4a). Additionally, the angle between Cl2-M2/Li4-Cl2 also indicates a movement of the apex chlorides (Figure S4c and S4d). However, the increasing zirconium content cannot be the primary driving force of the symmetry changes on M2/Li4 position because the M2/Li4 position is mainly lithium occupied with a fraction of zirconium and indium that is not changing significantly. Thus, the observed changes are more likely be induced by lithium which occupancy increases on the M2/Li4 site over the series of solid solution. However, the complete underlying reason for the changing distortion remains unclear.

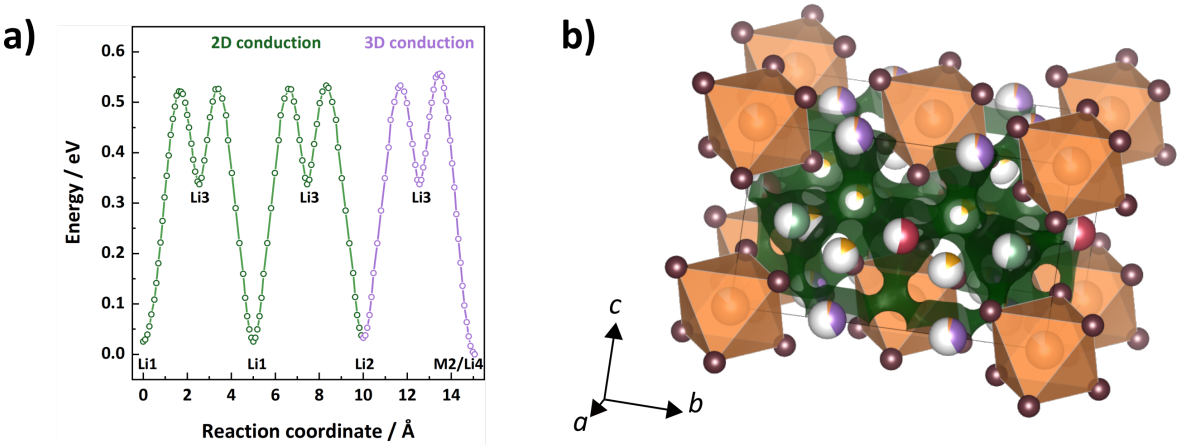

Figure 6: (a) Preferred lithium diffusion pathway of lithium through the structure calculated by a bond valence sum analysis. Li3 is an intermediate, higher energy state for the two-dimensional as well as for the three-dimensional diffusion between the jumps from the octahedral lithium position Li1, Li2 and M2/Li4. (b) Calculated isosurface for lithium ions in Li_3InCl_6. Possible trajectories for lithium-ion diffusion are displayed in green. The indium octahedra M1 are displayed all other polyhedra are omitted for simplicity.

Considering possible lithium diffusion pathways, within the monoclinic structure of Li_3InCl_6, these paths all need to occur via O_h - T_d - O_h. This is confirmed with ab initio molecular dynamics and bond valence sum calculations on Li^+ diffusion pathways from Wang *et al.* and Asano *et al.* for Li_3YBr_6, which exhibits the same body-centered cubic halide arrangement as Li_3InCl_6.[39,40] The tetrahedra within the crystal structure were identified as transition states for ionic motion. As, the site energy of the tetrahedron is relatively higher than the site energy of

the octahedron, the reduction of lithium ions *via* zirconium incorporation leads to the removal of lithium on the tetrahedral position Li3 first. The three-dimensional lithium-ion diffusion within $Li_{3-x}In_{1-x}Zr_xCl_6$ is possible because lithium can cross the (001) lattice plane through the M2/Li4 site (see Figure 1d), which is despite its low occupancy of another metal still a partially occupied lithium site. The three-dimensional diffusion should be influenced by the fraction of In^{3+}/Zr^{4+} on M2/Li4 site, as these can act as blocking defect in *c*-direction hindering the diffusion. Overall, lithium diffusion can be expected *via* Li1/Li2 - Li3 - M2/Li4 - Li3 - Li1/Li2 (see Figure 6), since the fraction of In^{3+}/Zr^{4+} on M2/Li4 site is low and blocking is minimized for this pathway.

Ionic transport. Temperature-dependent impedance spectroscopy and ^{7}Li NMR spin-lattice relaxometry experiments were performed to determine the transport properties of the solid solutions and to clarify the structural influences on ionic motion. Representative Nyquist plots of the substitution series $Li_{3-x}In_{1-x}Zr_xCl_6$ (x = 0, 0.2, 0.4) at 298 K are displayed in Figure 7a. The remaining room-temperature data are shown in the Supporting Information (Figure S5). In general at lower temperatures, the impedance spectra show suppressed semicircles and the capacitive blocking behavior of the electrodes. At elevated temperatures only the blocking behavior of the electrodes can be observed (see Figure S5). All impedance spectra at lower temperatures were fit with an equivalent circuit model (see inset Figure 7a) consisting of a parallel resistor-constant phase element (CPE) in series with a CPE representing a combined bulk and grain boundary processes and the blocking electrodes, respectively. In the impedance spectra recorded at elevated temperatures, only the capacitive behavior of the electrodes was fit. The determined ideality factors of the constant phase element range within 0.62 – 0.77 clearly indicating the presences of more than one process, e.g. grain and grain boundary.[49] Therefore, the different contributions of grain and grain boundary, cannot be deconvoluted in the impedance spectra, even at low temperatures of −40 °C. Thus, the herein reported conductivity values represent total conductivities. All six compositions exhibit Arrhenius behavior in the measured temperature range (see Figure 7b). The room-temperature conductivity and activation energy were calculated from the linear Arrhenius fit (see Figure 7c and 7d). The introduction of zirconium into the crystal structure of Li_3InCl_6 clearly has a beneficial impact on the conductivity. The already high room-temperature conductivity of Li_3InCl_6 of 0.47 mS·cm^{-1} was improved to 1.25 mS·cm^{-1} for $Li_{2.6}In_{0.6}Zr_{0.4}Cl_6$. However, reported conductivities of Li_3InCl_6 are higher and range between 1.5 mS·cm^{-1} – 2 mS·cm^{-1}.[24,25,35] The differences in conductivity may stem from the varying synthesis parameters and

annealing times that were applied, since it is known for the halide materials that synthesis conditions have a severe influence on structure and properties.[29,31,32,50] In addition, the small conductivity discrepancy may also be due to the known interlaboratory deviations in the ionic conductivity of these mechanically soft materials.[51] The activation energy determined by impedance spectroscopy reaches a minimum for $Li_{2.6}In_{0.6}Zr_{0.4}Cl_6$ which coincides with the optimum of the conductivity found here.

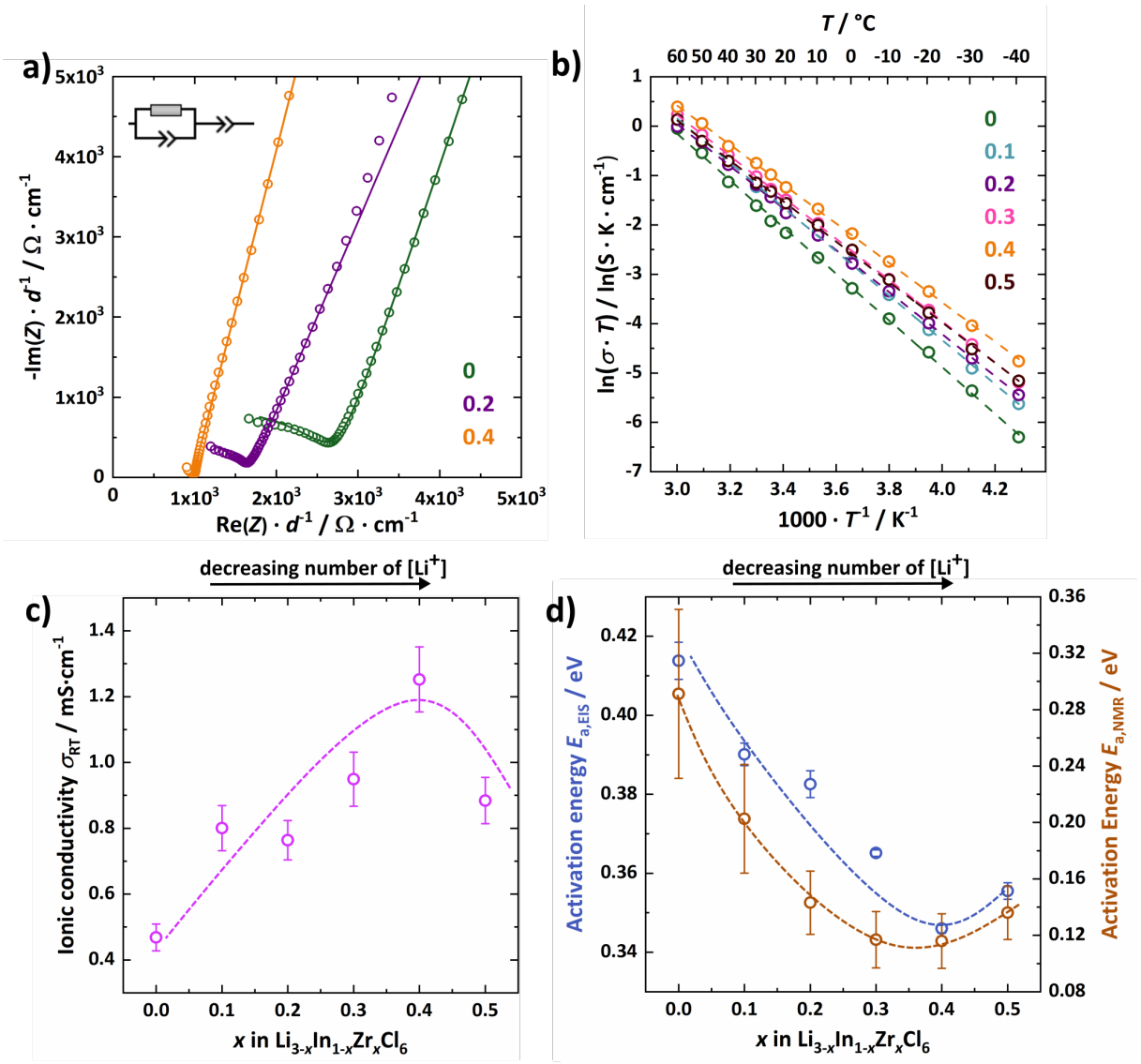

Figure 7: a) Display of exemplary impedance spectra for $Li_{3-x}In_{1-x}Zr_xCl_6$ (x = 0, 0.2, 0.4) at 298 K with the used equivalent circuit model as inset. The impedance spectra are normalized to the pellet thickness for visual comparison. b) Arrhenius plot of the substitution series. All substitutions show a linear behavior over the measured temperature range. (c) The room-temperature conductivities and (d) activation energies of impedance (blue) as well as ^{7}Li NMR T_1 relaxometry (brown) measurements as a function of zirconium content in $Li_{3-x}In_{1-x}Zr_xCl_6$ are

displayed. The lines in a) and b) are actual fits, while in c) and d) the lines are guides-to-the-eye.

In order to corroborate this minimum observed from impedance spectroscopy, the activation energy is also determined by spin-lattice relaxation ^{7}Li NMR, shown in Figure S6. The modified Bloembergen-Purcell-Pound (BPP) model[52,53] was used to calculate the activation energies (see Figure 7d) which follow a similar trend, although in general slightly smaller compared to the activation energy obtained by impedance spectroscopy. In addition, the spin-lattice ^{7}Li relaxation data (Figure S6) shows two different dynamical modes at elevated temperatures, each of which corresponds to a Li^+ jump process. The mode occurring at higher temperatures shifts with increasing zirconium content into the mode at lower temperature indicating that the jump processes adapt to each other. Gombotz *et al.* measured spin-lattice ^{7}Li NMR relaxometry for Li_3YBr_6, which exhibits the same crystal structure as Li_3InCl_6 albeit showing a different cation ordering.[38] When monitoring the temperature dependence of $1/T_1$, an abrupt change in $1/T_1$ was observed at 273 K, in form of a discontinuation of the data, which was attributed to structural changes. At higher temperatures the characteristic rate peak of solid electrolytes was observed, however, there is no second mode present as observed here for Li_3InCl_6, suggesting that a different jump process occurs on a similar timescale within Li_3YBr_6.

Taken together, the lithium content is reduced by zirconium introduction, resulting in the introduction of further vacancies into the structure. Thus, the number of available sites for ionic jumps increases. The optimal vacancy density for this substitution series seems to be for $Li_{2.6}In_{0.6}Zr_{0.4}Cl_6$ which corresponds to $\sim 1.9 \cdot 10^{21}$ vacancies·cm^{-3}. A positive impact of vacancies on the conductivity was already observed in several halide compositions $Li_{3-x}Er_{1-x}Zr_xCl_6$, $Li_{3-x}Y_{1-x}Zr_xCl_6$, Li_xScCl_{3+x}, $Li_{2.25}Zr_{0.75}Fe_{0.25}Cl_6$ and sodium analogue $Na_{3-x}Er_{1-x}Zr_xCl_6$.[26,27,33,48] However, here the enhancement of the conductivity may not only arise from the decrease of lithium ion concentration but also from the changes to the lithium substructure that includes a cation-site disorder on M2/Li4 site, leading to more Li^+ on this site further simplifying a three-dimensional diffusion.

4. Conclusion

In this work we report the series of solid solutions $Li_{3-x}In_{1-x}Zr_xCl_6$ ($0 \leq x(Zr) \leq 0.5$) prepared *via* mechanochemical synthesis. A new lithium substructure was proposed for Li_3InCl_6 introducing a cation-site disorder on M2/Li4 as well as a tetrahedrally coordinated site Li3 that results in an observed three-dimensional lithium polyhedral network. The substitution with Zr induced a non-uniform volume change that can be linked to changing M2/Li4 octahedral distortions. An

increasing conductivity is found with a concurrent reduction of the activation barrier suggesting that the increasing vacancy concentration beneficially affects the ionic transport. Nevertheless, by changing the composition of adding more Zr^{4+} and reducing the Li^{+} content, a structural redistribution of Li^{+} is found that may suggest a stronger three-dimensional diffusion behavior along the *c*-direction.

If this redistribution of Li^{+} into the three-dimensional pathways is due to induced structural changes by incorporating Zr^{4+} together with the electrostatic influences of a highly charged cation, or if it just reflects the higher ionic conductivity of the material itself remains an open question. Furthermore, systematic investigations are required to explore the influence of the local structural distortions on the ionic transport of halides as here changes from the initial distortions seem to enhance ionic conductivity. This work shows how to further improve the ionic transport in these superionic halide materials and is a first step to understand the intricate relationships of composition, structure and ionic transport in this class of materials.

Acknowledgments

The research was supported by the Federal Ministry of Education and Research (BMBF) within the project EProFest under grant number 03XP0346E. A.B. gratefully acknowledges the Alexander von Humboldt Foundation for financial support through a Postdoctoral Fellowship. B.W. is member of the International Graduate School for Battery Chemistry, Characterization, Analysis, Recycling and Application (BACCARA), which is funded by the Ministry for Culture and Science of North Rhine Westphalia, Germany.

Supporting Information

The supporting information includes laboratory X-ray diffraction data, neutron diffraction data, Rietveld refinement results, structural evolution of polyhedral and occupancy changes of M2/Li4 site, temperature-dependent impedance spectra, nuclear magnetic resonance data and the crystallographic information files (CIF).

References

(1) Janek, J.; Zeier, W. G. A Solid Future for Battery Development. *Nat. Energy* **2016**, *1* (9), 16141.

(2) Famprikis, T.; Canepa, P.; Dawson, J. A.; Islam, M. S.; Masquelier, C. Fundamentals of Inorganic Solid-State Electrolytes for Batteries. *Nat. Mater.* **2019**, *18*, 1278–1291.

(3) Murugan, R.; Thangadurai, V.; Weppner, W. Fast Lithium Ion Conduction in Garnet-Type $Li_7La_3Zr_2O_{12}$. *Angew. Chemie Int. Ed.* **2007**, *46* (41), 7778–7781.

(4) Lu, Y.; Meng, X.; Alonso, J. A.; Fernández-Díaz, M. T.; Sun, C. Effects of Fluorine Doping on Structural and Electrochemical Properties of $Li_{6.25}Ga_{0.25}La_3Zr_2O_{12}$ as Electrolytes for Solid-State Lithium Batteries. *ACS Appl. Mater. Interfaces* **2019**, *11* (2), 2042–2049.

(5) Cussen, E. J. Structure and Ionic Conductivity in Lithium Garnets. *J. Mater. Chem.* **2010**, *20* (25), 5167–5173.

(6) Kamaya, N.; Homma, K.; Yamakawa, Y.; Hirayama, M.; Kanno, R.; Yonemura, M.; Kamiyama, T.; Kato, Y.; Hama, S.; Kawamoto, K.; et al. A Lithium Superionic Conductor. *Nat. Mater.* **2011**, *10* (9), 682–686.

(7) Kato, Y.; Saito, R.; Sakano, M.; Mitsui, A.; Hirayama, M.; Kanno, R. Synthesis, Structure and Lithium Ionic Conductivity of Solid Solutions of $Li_{10}(Ge_{1-x}M_x)P_2S_{12}$ (M = Si, Sn). *J. Power Sources* **2014**, *271*, 60–64.

(8) Bron, P.; Johansson, S.; Klaus, Z.; Schmedt auf der Günne, J.; Dehnen, S.; Roling, B. $Li_{10}SnP_2S_{12}$: An Affordable Lithium Superionic Conductor. *J. Am. Chem. Soc.* **2013**, *135* (42), 15694–15697.

(9) Kraft, M. A.; Culver, S. P.; Calderon, M.; Böcher, F.; Krauskopf, T.; Senyshyn, A.;

Dietrich, C.; Zevalkink, A.; Janek, J.; Zeier, W. G. Influence of Lattice Polarizability on the Ionic Conductivity in the Lithium Superionic Argyrodites Li_6PS_5X (X = Cl, Br, I). *J. Am. Chem. Soc.* **2017**, *139* (31), 10909–10918.

(10) Deiseroth, H.-J.; Kong, S.-T.; Eckert, H.; Vannahme, J.; Reiner, C.; Zaiß, T.; Schlosser, M. Li_6PS_5X: A Class of Crystalline Li-Rich Solids With an Unusually High Li^+ Mobility. *Angew. Chemie* **2008**, *120* (4), 767–770.

(11) Zhou, L.; Assoud, A.; Zhang, Q.; Wu, X.; Nazar, L. F. New Family of Argyrodite Thioantimonate Lithium Superionic Conductors. *J. Am. Chem. Soc.* **2019**, *141*, 19002–19013.

(12) Kanno, R.; Murayama, M. Lithium Ionic Conductor Thio-LISICON: The Li_2S-GeS_2-P_2S_5 System. *J. Electrochem. Soc.* **2001**, *148* (7), 742–746.

(13) Murayama, M.; Sonoyama, N.; Yamada, A.; Kanno, R. Material Design of New Lithium Ionic Conductor, Thio-LISICON, in the Li_2S-P_2S_5 System. *Solid State Ionics* **2004**, *170* (3–4), 173–180.

(14) Minafra, N.; Hogrefe, K.; Barbon, F.; Helm, B.; Li, C.; Wilkening, H. M. R.; Zeier, W. G. Two-Dimensional Substitution: Toward a Better Understanding of the Structure–Transport Correlations in the Li-Superionic Thio-LISICONs. *Chem. Mater.* **2021**, *33* (2), 727–740.

(15) Kaib, T.; Haddadpour, S.; Kapitein, M.; Bron, P.; Schröder, C.; Eckert, H.; Roling, B.; Dehnen, S. New Lithium Chalcogenidotetrelates, LiChT: Synthesis and Characterization of the Li^+-Conducting Tetralithium Ortho-Sulfidostannate Li_4SnS_4. *Chem. Mater.* **2012**, *24* (11), 2211–2219.

(16) Ohno, S.; Banik, A.; Dewald, G. F.; Kraft, M. A.; Krauskopf, T.; Minafra, N.; Till, P.; Weiss, M.; Zeier, W. G. Materials Design of Ionic Conductors for Solid State Batteries.

Prog. Energy **2020**, *2* (2), 022001.

(17) Krauskopf, T.; Culver, S. P.; Zeier, W. G. Bottleneck of Diffusion and Inductive Effects in $Li_{10}Ge_{1-x}Sn_xP_2S_{12}$. *Chem. Mater.* **2018**, *30* (5), 1791–1798.

(18) Muy, S.; Voss, J.; Schlem, R.; Koerver, R.; Sedlmaier, S. J.; Maglia, F.; Lamp, P.; Zeier, W. G.; Shao-Horn, Y. High-Throughput Screening of Solid-State Li-Ion Conductors Using Lattice-Dynamics Descriptors. *iScience* **2019**, *16*, 270–282.

(19) Muy, S.; Bachman, J. C.; Giordano, L.; Chang, H.-H.; Abernathy, D. L.; Bansal, D.; Delaire, O.; Hori, S.; Kanno, R.; Maglia, F.; et al. Tuning Mobility and Stability of Lithium Ion Conductors Based on Lattice Dynamics. *Energy Environ. Sci.* **2018**, *11* (4), 850–859.

(20) Culver, S. P.; Koerver, R.; Krauskopf, T.; Zeier, W. G. Designing Ionic Conductors: The Interplay between Structural Phenomena and Interfaces in Thiophosphate-Based Solid-State Batteries. *Chem. Mater.* **2018**, *30* (13), 4179–4192.

(21) Ohno, S.; Helm, B.; Fuchs, T.; Dewald, G.; Kraft, M. A.; Culver, S. P.; Senyshyn, A.; Zeier, W. G. Further Evidence for Energy Landscape Flattening in the Superionic Argyrodites $Li_{6+x}P_{1-x}M_xS_5I$ (M = Si, Ge, Sn). *Chem. Mater.* **2019**, *31* (13), 4936–4944.

(22) Kraft, M. A.; Ohno, S.; Zinkevich, T.; Koerver, R.; Culver, S. P.; Fuchs, T.; Senyshyn, A.; Indris, S.; Morgan, B. J.; Zeier, W. G. Inducing High Ionic Conductivity in the Lithium Superionic Argyrodites $Li_{6+x}P_{1-x}Ge_xS_5I$ for All-Solid-State Batteries. *J. Am. Chem. Soc.* **2018**, *140* (47), 16330–16339.

(23) Zhou, L.; Kwok, C. Y.; Shyamsunder, A.; Zhang, Q.; Wu, X.; Nazar, L. F. A New Halospinel Superionic Conductor for High-Voltage All Solid State Lithium Batteries. *Energy Environ. Sci.* **2020**, *13* (7), 2056–2063.

(24) Li, X.; Liang, J.; Luo, J.; Norouzi Banis, M.; Wang, C.; Li, W.; Deng, S.; Yu, C.; Zhao, F.; Hu, Y.; et al. Air-Stable Li_3InCl_6 Electrolyte with High Voltage Compatibility for All-Solid-State Batteries. *Energy Environ. Sci.* **2019**, *12* (9), 2665–2671.

(25) Li, X.; Liang, J.; Chen, N.; Luo, J.; Adair, K. R.; Wang, C.; Banis, M. N.; Sham, T.; Zhang, L.; Zhao, S.; et al. Water-Mediated Synthesis of a Superionic Halide Solid Electrolyte. *Angew. Chemie* **2019**, *131* (46), 16579–16584.

(26) Park, K.-H.; Kaup, K.; Assoud, A.; Zhang, Q.; Wu, X.; Nazar, L. F. High-Voltage Superionic Halide Solid Electrolytes for All-Solid-State Li-Ion Batteries. *ACS Energy Lett.* **2020**, *5* (2), 533–539.

(27) Liang, J.; Li, X.; Wang, S.; Adair, K. R.; Li, W.; Zhao, Y.; Wang, C.; Hu, Y.; Zhang, L.; Zhao, S.; et al. Site-Occupation-Tuned Superionic Li_xScCl_{3+x} Halide Solid Electrolytes for All-Solid-State Batteries. *J. Am. Chem. Soc.* **2020**, *142* (15), 7012–7022.

(28) Schlem, R.; Bernges, T.; Li, C.; Kraft, M. A.; Minafra, N.; Zeier, W. G. Lattice Dynamical Approach for Finding the Lithium Superionic Conductor Li_3ErI_6. *ACS Appl. Energy Mater.* **2020**, *3* (4), 3684–3691.

(29) Schlem, R.; Muy, S.; Prinz, N.; Banik, A.; Shao-Horn, Y.; Zobel, M.; Zeier, W. G. Mechanochemical Synthesis: A Tool to Tune Cation Site Disorder and Ionic Transport Properties of Li_3MCl_6 (M = Y, Er) Superionic Conductors. *Adv. Energy Mater.* **2020**, *10* (6), 1903719.

(30) Riegger, L. M.; Schlem, R.; Sann, J.; Zeier, W. G.; Janek, J. Lithium-Metal Anode Instability of the Superionic Halide Solid Electrolytes and the Implications for Solid-State Batteries. *Angew. Chemie Int. Ed.* **2021**, *60*, 6792–6797.

(31) Schlem, R.; Banik, A.; Ohno, S.; Suard, E.; Zeier, W. G. Insights into the Lithium Sub-Structure of Superionic Conductors Li_3YCl_6 and Li_3YBr_6. *Chem. Mater.* **2021**, *33* (1),

327–337.

(32) Yu, C.; Li, Y.; Adair, K. R.; Li, W.; Goubitz, K.; Zhao, Y.; Willans, M. J.; Thijs, M. A.; Wang, C.; Zhao, F.; et al. Tuning Ionic Conductivity and Electrode Compatibility of Li_3YBr_6 for High-Performance All Solid-State Li Batteries. *Nano Energy* **2020**, *77*, 105097.

(33) Kwak, H.; Han, D.; Lyoo, J.; Park, J.; Jung, S. H.; Han, Y.; Kwon, G.; Kim, H.; Hong, S. T.; Nam, K. W.; et al. New Cost-Effective Halide Solid Electrolytes for All-Solid-State Batteries: Mechanochemically Prepared Fe^{3+}-Substituted Li_2ZrCl_6. *Adv. Energy Mater.* **2021**, *11* (12), 2003190.

(34) Steiner, H.-J.; Lutz, H. D. Neue Schnelle Ionenleiter Vom Typ $M^I_3M^{III}Cl_6$ (M^I = Li, Na, Ag; M^{III} = In, Y). *Zeitschrift für Anorg. und Allg. Chemie* **1992**, *613* (7), 26–30.

(35) Li, X.; Liang, J.; Adair, K. R.; Li, J.; Li, W.; Zhao, F.; Hu, Y.; Sham, T.-K.; Zhang, L.; Zhao, S.; et al. Origin of Superionic $Li_3Y_{1-x}In_xCl_6$ Halide Solid Electrolytes with High Humidity Tolerance. *Nano Lett.* **2020**, *20* (6), 4384–4392.

(36) Sacci, R. L.; Bennett, T. H.; Drews, A. R.; Anandan, V.; Kirkham, M. J.; Daemen, L. L.; Nanda, J. Phase Evolution during Lithium-Indium Halide Superionic Conductor Dehydration. *J. Mater. Chem. A* **2021**, *9*, 990–996.

(37) Schmidt, M. O.; Wickleder, M. S.; Meyer, G. Zur Kristallstruktur von Li_3InCl_6. *Zeitschrift für Anorg. und Allg. Chemie* **1999**, *625* (4), 539–540.

(38) Gombotz, M.; Wilkening, H. M. R. Fast Li Ion Dynamics in the Mechanosynthesized Nanostructured Form of the Solid Electrolyte Li_3YBr_6. *ACS Sustain. Chem. Eng.* **2021**, *9* (2), 743–755.

(39) Wang, S.; Bai, Q.; Nolan, A. M.; Liu, Y.; Gong, S.; Sun, Q.; Mo, Y. Lithium Chlorides

and Bromides as Promising Solid-State Chemistries for Fast Ion Conductors with Good Electrochemical Stability. *Angew. Chemie Int. Ed.* **2019**, *58* (24), 8039–8043.

(40) Asano, T.; Sakai, A.; Ouchi, S.; Sakaida, M.; Miyazaki, A.; Hasegawa, S. Solid Halide Electrolytes with High Lithium-Ion Conductivity for Application in 4 V Class Bulk-Type All-Solid-State Batteries. *Adv. Mater.* **2018**, *30* (44), 1803075.

(41) Shannon, R. D. Revised Effective Ionic Radii and Systematic Studies of Interatomic Distances in Halides and Chalcogenides. *Acta Crystallogr. Sect. A* **1976**, *32* (5), 751–767..

(42) Park, D.; Park, H.; Lee, Y.; Kim, S. O.; Jung, H. G.; Chung, K. Y.; Shim, J. H.; Yu, S. Theoretical Design of Lithium Chloride Superionic Conductors for All-Solid-State High-Voltage Lithium-Ion Batteries. *ACS Appl. Mater. Interfaces* **2020**, *12* (31), 34806–34814.

(43) Coelho, A. A. *TOPAS-Academic* **2007**, *Brisbane*.

(44) Huq, A.; Kirkham, M.; Peterson, P. F.; Hodges, J. P.; Whitfield, P. S.; Page, K.; Hűgle, T.; Iverson, E. B.; Parizzi, A.; Rennich, G. POWGEN: Rebuild of a Third-Generation Powder Diffractometer at the Spallation Neutron Source. *J. Appl. Crystallogr.* **2019**, *52* (5), 1189–1201.

(45) Zhang, W.; Weber, D. A.; Weigand, H.; Arlt, T.; Manke, I.; Schröder, D.; Koerver, R.; Leichtweiss, T.; Hartmann, P.; Zeier, W. G.; et al. Interfacial Processes and Influence of Composite Cathode Microstructure Controlling the Performance of All-Solid-State Lithium Batteries. *ACS Appl. Mater. Interfaces* **2017**, *9* (21), 17835–17845.

(46) Chen, H.; Wong, L. L.; Adams, S. SoftBV – a Software Tool for Screening the Materials Genome of Inorganic Fast Ion Conductors. *Acta Crystallogr.* **2019**, *B75* (1), 18–33.

(47) Chen, H.; Adams, S. Bond Softness Sensitive Bond-Valence Parameters for Crystal Structure Plausibility Tests. *IUCrJ* **2017**, *4* (5), 614–625.

(48) Schlem, R.; Banik, A.; Eckardt, M.; Zobel, M.; Zeier, W. G. $Na_{3-x}Er_{1-x}Zr_xCl_6$ - A Halide-Based Fast Sodium-Ion Conductor with Vacancy-Driven Ionic Transport. *ACS Appl. Energy Mater.* **2020**, *3* (10), 10164–10173.

(49) Brug, G. J.; van den Eeden, A. L. G.; Sluyters-Rehbach, M.; Sluyters, J. H. The Analysis of Electrode Impedances Complicated by the Presence of a Constant Phase Element. *J. Electroanal. Chem. Interfacial Electrochem.* **1984**, *176* (1–2), 275–295.

(50) Banik, A.; Famprikis, T.; Ghidiu, M.; Ohno, S.; Kraft, M. A.; Zeier, W. G. On the Underestimated Influence of Synthetic Conditions in Solid Ionic Conductors. *Chem. Sci.* **2021**. https://doi.org/10.1039/D0SC06553F.

(51) Ohno, S.; Bernges, T.; Buchheim, J.; Duchardt, M.; Hatz, A. K.; Kraft, M. A.; Kwak, H.; Santhosha, A. L.; Liu, Z.; Minafra, N.; et al. How Certain Are the Reported Ionic Conductivities of Thiophosphate-Based Solid Electrolytes? An Interlaboratory Study. *ACS Energy Lett.* **2020**, *5* (3), 910–915.

(52) Bloembergen, N.; Purcell, E. M.; Pound, R. V. Relaxation Effects in Nuclear Magnetic Resonance Absorption. *Phys. Rev.* **1948**, *73* (7), 679–712.

(53) Arbi, K.; Lazarraga, M. G.; Ben Hassen Chehimi, D.; Ayadi-Trabelsi, M.; Rojo, J. M.; Sanz, J. Lithium Mobility in $Li_{1.2}Ti_{1.8}R_{0.2}(PO_4)_3$ Compounds (R = Al, Ga, Sc, In) as Followed by NMR and Impedance Spectroscopy. *Chem. Mater.* **2004**, *16* (2), 255–262.

For Table of Contents only